coatings

Article

Microstructure and Mechanical Properties of TiC/TiB Composite Ceramic Coatings In-Situ Synthesized by Ultrasonic Vibration-Assisted Laser Cladding

Hangbiao Mi [1,†]**, Tao Chen** [2,†]**, Zixin Deng** [1]**, Shengchen Li** [1]**, Jian Liu** [1] **and Defu Liu** [1,3,*]

[1] College of Mechanical and Electrical Engineering, Central South University, Changsha 410083, China; mihangbiao@csu.edu.cn (H.M.); zixindeng66@csu.edu.cn (Z.D.); xcshengcli@csu.edu.cn (S.L.); liujian317@csu.edu.cn (J.L.)

[2] School of Mechanical Engineering and Rail Transit, Changzhou University, Changzhou 213164, China; ctxy999@126.com

[3] State Key Laboratory of High Performance Complex Manufacturing, Changsha 410083, China

[*] Correspondence: liudefu@csu.edu.cn

[†] These authors contributed equally to the work.

Abstract: Laser cladding coating has many advantages in surface modification, such as a small heat-affected zone, and good metallurgical bonding. However, some serious problems such as pores, and poor forming quality still exist in the coating. To suppress these problems, a novel process of ultrasonic vibration-assisted laser cladding process was adopted to in-situ synthesize TiC/TiB composite ceramic coating on the surface of titanium alloy. Results showed that the introduction of ultrasonic vibration effectively improved the surface topography of the coating, reduced the number of pores in the coating, refined the crystal grains of the coating, decreased the residual tensile stress in the coating, and increased the micro-hardness of the coating. The tribological properties of the coating were significantly improved by the ultrasonic vibration, the wear resistance of the coating fabricated with ultrasonic vibration at power of 400 W increased about 1.2 times compared with the coating fabricated without ultrasonic vibration, and the friction coefficient decreased by 50%.

Keywords: ultrasonic vibration; laser cladding; microstructures; wear resistance; residual stress

1. Introduction

Titanium alloy has excellent biomechanical properties, outstanding formability and machinability, good corrosion resistance and favourable biocompatibility, which has been widely used in the field of artificial joint replacement [1]. However, due to the poor tribological properties of the titanium alloy surface, the wear debris generated by wear in the human body will seriously affect the service life of the artificial hip joint [2,3]. Therefore, it is crucial to develop artificial hip joints with high longevity and excellent tribological properties. Currently, surface modification techniques such as plasma spraying [4–7] and laser cladding [8–11] can be used to improve the tribological properties and maintain the excellent mechanical properties by preparing a layer of bioinert ceramic coating on the surface of the titanium alloy artificial hip joint head, which in turn meets the long-life requirements of the artificial hip joint.

At present, to further obtain better wear resistance of the coating, some researchers have improved the coating quality by utilizing the methods such as optimizing the laser cladding process parameters, preheating or post-heat treatment. Erfanmanesh et al. [12] and Zhang et al. [13] obtained metal-ceramic composite coatings with no cracks and good metallurgical bonding by optimizing the laser cladding process parameters. Liu et al. [14] fabricated high-entropy alloy coatings without crack by laser cladding process through preheating the substrate. Indeed, our previous results show that [15] TiC/TiB bioinert composite ceramic coating was in-situ synthesized on the surface of Ti6Al4V titanium alloy

by the laser cladding process, which significantly improved wear resistance of the titanium alloy surface, and the residual stress and crack sensitivity of the coating were reduced via post-heat treatment. However, using conventional laser cladding to prepare ceramic coatings has its own disadvantages that are difficult to overcome, such as poor coating surface forming quality, internal defects and uneven distribution of ceramic crystal grains in the coating. Optimization of the process parameters alone is not able to improve the crystal grain distribution in the coating. Preheating treatment may cause microstructure coarsening of the coating [16], and the post-heat treatment of the coating does not improve the internal defects of the coating. Relying on a single laser cladding process cannot effectively solve these problems. In order to solve the above problems and further improve the tribological properties of the coating, we introduced ultrasonic vibration into the laser cladding process based on the original experiments, and used ultrasonic vibration-assisted laser cladding process to prepare ceramic coatings.

In recent years, ultrasonic vibration technology has been applied in laser engineering net shaping of ceramic and metal parts [17–19] and preparation of metal-based coatings by laser cladding [20–22] due to its characteristics such as refining crystal grains, reducing macro/micro defects, and improving mechanical properties. Cong et al. [17–19] proposed to use ultrasonic vibration-assisted laser net shaping to avoid the manufacturing defects of metal and ceramic parts, and found that ultrasonic vibration could reduce porosity, refine crystal grain size, and improve mechanical properties such as hardness. Zhu et al. [20] prepared Inconel 718 coatings by ultrasonic vibration-assisted laser cladding process, which reduced the number and size of pores in the coatings, increased the nucleation rate during the metal solidification process, refined the crystal grains, and thus improved the hardness and wear resistance of the coating. Ma et al. [21] studied the effects of ultrasonic vibration on the microstructure and mechanical properties of yttria stabilized zirconia (YSZ) coatings by laser cladding process. They found that the equiaxed crystal grain size in the coating decreased with the increase of ultrasonic vibration power, the distribution of each element in the coating was more uniform, and the friction coefficient of the coating was reduced. Wang et al. [22] prepared ceramic particle-reinforced iron-based coatings by ultrasonic vibration-assisted laser cladding. They found that the ceramic crystal grain of the coating fabricated with ultrasonic vibration was refined, the ceramic phase content in the coating was increased, the surface morphology quality of the coating was improved, and the hardness and wear resistance of the coating were enhanced, but the dilution rate of the coating was slightly increased, compared with the coating fabricated without ultrasonic vibration. In summary, the ultrasonic vibration-assisted laser cladding process can improve the coating's morphological quality, reduce the number of pores in the coating, and refine the crystal grain size in the coating. Therefore, the ultrasonic vibration is introduced into the laser cladding process to prepare ceramic coating, which has the advantages in improving the quality and performance of the coating.

In this paper, ultrasonic vibration with a frequency of 20 kHz was introduced into the molten pool through an amplitude transformer by using the ultrasonic vibration-assisted laser cladding process, and a TiC/TiB composite bioinert wear-resistant ceramic coating was prepared on the Ti6Al4V alloy surface by in-situ synthesis with mixed B_4C powder and Ti powder as cladding raw material. The microstructure, phase composition, micro-hardness, wear resistance, and residual stress of the coatings prepared by applying different ultrasonic vibration powers were investigated in detail via scanning electron microscopy (SEM), energy dispersive spectroscopy (EDS), X-ray diffraction (XRD), micro-hardness tester, and friction and wear tester. The forming mechanism of TiC/TiB composite coating in-situ synthesized by ultrasonic vibration-assisted laser cladding process was also analyzed. Using the advantages of ultrasonic vibration-assisted laser cladding technology, the microstructure of ceramic coatings can be effectively improved, which gives the coatings excellent mechanical and tribological properties.

2. Materials and Methods

2.1. Experimental Material Selection and Treatment

The Ti6Al4V medical titanium alloy (Baoji INT Titanium Medical Co., Ltd., Baoji, China) was used as the substrate material for laser cladding, and the sample size was 30 mm × 30 mm × 6 mm. Ti powder (purity > 99.9%, average particle size 5 μm, Naiou Nano Technology Co., Ltd., Shanghai, China) and B_4C powder (purity > 99.9%, average particle size 50 nm, Naiou Nano Technology Co., Ltd., Shanghai, China) were used as the cladding powders. The micro morphology images of Ti powder and B_4C powder observed using scanning electron microscopy (SEM) are shown in Figure 1a,b, respectively.
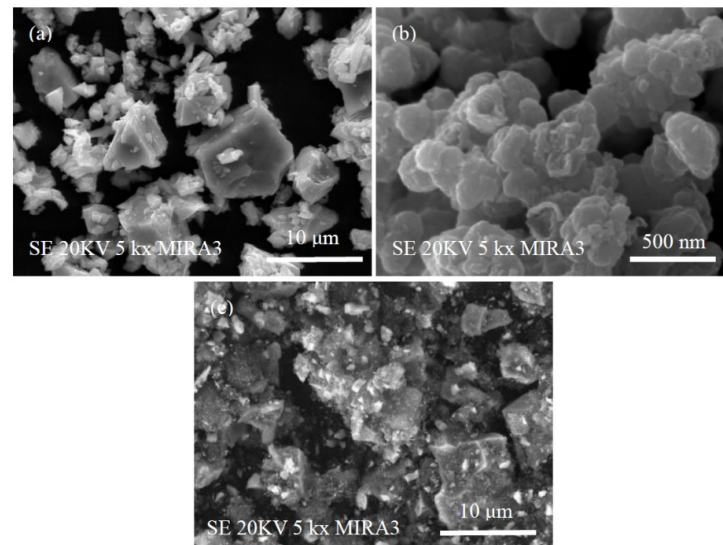

Figure 1. SEM images of powders: (**a**) Ti micro-particle powder, (**b**) B_4C nano-particle powder, (**c**) Ti and B_4C mixed powder.

The substrates were polished with 80 #, 120 #, 240 #, 320 #, 600 # SiC sandpaper to remove the oxide layer on the surface, and placed in deionized water and ethanol absolute respectively to be cleaned by using an ultrasonic cleaning machine (Shenzhen Jiemeng Cleaning Equipment Co., Ltd., Shenzhen, China), then dried naturally for 10 min before test. The Ti powder and B_4C powder were mixed in a mass ratio of 7:3 [15], and the powder was mixed thoroughly using a planetary ball mill (Hunan Chuangweilai Electromechanical Equipment Manufacturing Co., Ltd., Yueyang, China) at 200 rpm for 3 h. The microscopic morphology of the mixed powder is shown in Figure 1c. Then, 0.4 g mixed powder was added to 2 mL of aqueous polyvinyl alcohol solution with a concentration of 2 vol.%, and the mixture was stirred to a viscous consistency, which was uniformly pre-placed on a substrate top surface. The thickness of the pre-placed powder layer was about 0.4 mm. After that, the substrates with the mixed powder layer were pre-dried at a constant temperature heating platform (Dongguan Shenwu Electronic Technology Co., Ltd., Dongguan, China) at 70 °C for 30 min, and then put into a vacuum drying oven (Shenzhen Aiske Instrument Equipment Co., Ltd., Shenzhen, China) for continuous drying at 50 °C for 12 h.

2.2. Ultrasonic Vibration-Assisted Laser Cladding Set-Up

The schematic diagram of the ultrasonic vibration-assisted laser cladding system is shown in Figure 2a, which is mainly composed of a laser system, a motion control system, a computer control system, an ultrasonic vibration system, and some auxiliary devices. The laser system consists of an RFL-500 fiber laser (Wuhan Raycus Fiber Laser Technologies Co., Ltd., Wuhan, China) and a focusing system [23]. The motion control system controls the movement of the X-Y axis of the substrate and adjusts the spot size through the movement of the Z axis. The ultrasonic vibration system includes an ultrasonic generator, and an ultrasonic vibration device which comprises ultrasonic transducer, ultrasonic transformer

(horn), fixture, etc. The ultrasonic transducer is driven by the high frequency (20 kHz) electrical energy from the ultrasonic generator, which can convert the electrical energy into ultrasonic vibration in vertical direction. In order to ensure the stability of the ultrasonic vibration device, an ultrasonic generator (Dawei Ultrasonic Equipment Co., Ltd., Shaoxing, China) which can realize automatic frequency tracking was selected, whose ultrasonic output frequency is 20 kHz and output power is adjustable from 200 to 2000 W. In order to realize the effect of ultrasonic vibration on the laser cladding molten pool, the ultrasonic vibration was transmitted to the surface of the substrate via ultrasonic transformer. At the same time, since the substrate needs to be replaced frequently, the substrate is fixed to the end of the horn through a fixture. The schematic diagram of the ultrasonic vibration device is shown in Figure 2b.
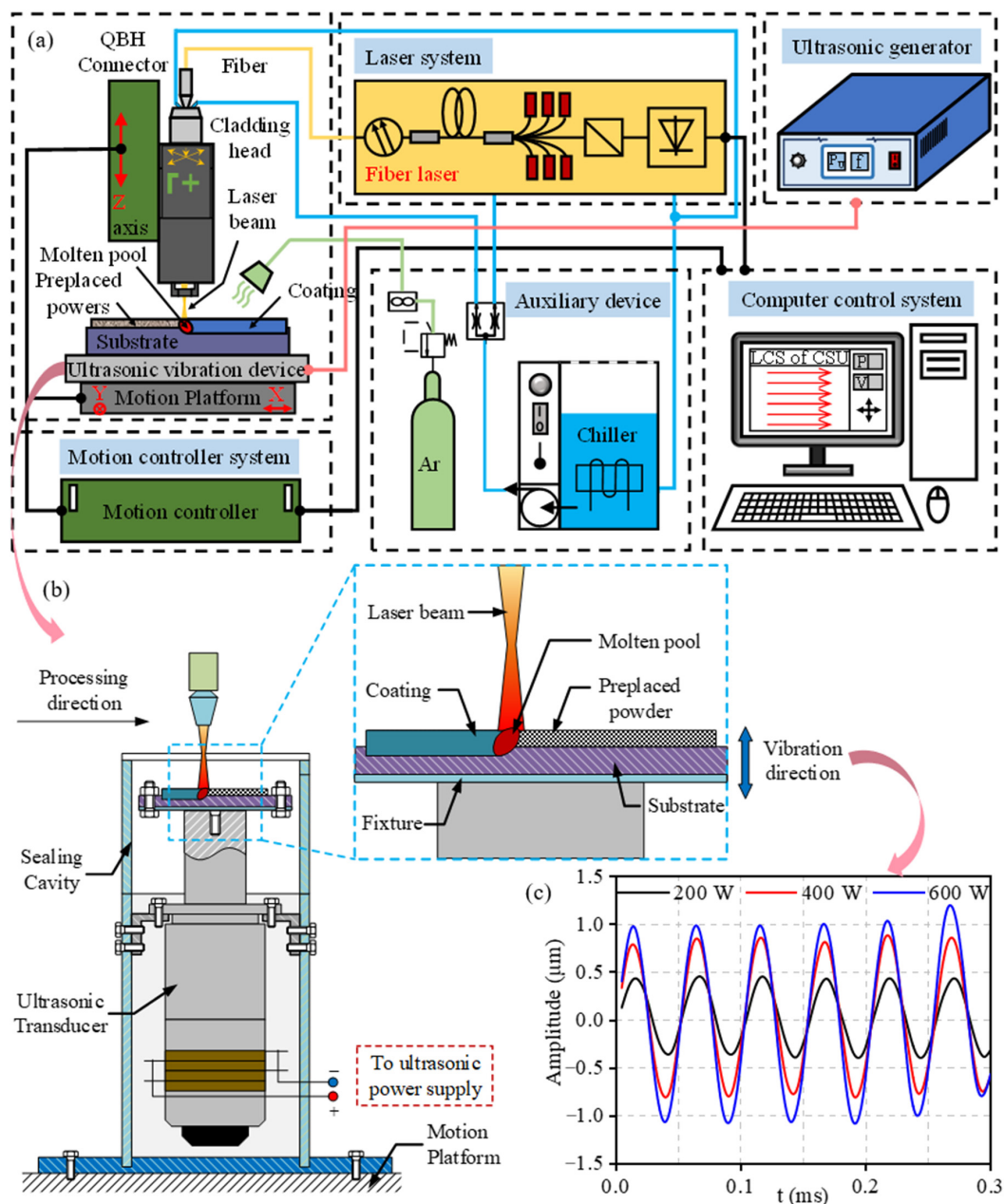
Figure 2. (**a**) Schematic diagram of ultrasonic vibration-assisted laser cladding system, (**b**) Schematic diagram of ultrasonic vibration device, (**c**) Ultrasonic vibration waveforms of substrate top surface with different ultrasonic vibration powers.

A high-precision laser displacement sensor (LK-G5001V, Keyence, Osaka, Japan) was used to measure the amplitude of the substrate top surface clamped to the end of the horn by a fixture. Figure 2c shows the ultrasonic vibration waveform of the substrate at different ultrasonic vibration power. It is observed that the amplitudes of substrate top surface were about 0.4, 0.8 and 1 μm when the ultrasonic power was 200, 400 and 600 W respectively.

2.3. Ultrasonic Vibration-Assisted Laser Cladding Process

Experimental parameters of ultrasonic vibration-assisted laser cladding process for fabricating TiC/TiB composite ceramic coatings are shown in Table 1. A total of 42 tracks of side-by-side overlapping cladding were performed on the substrate surface with an overlap rate of 40%. The laser cladding process was carried out in a protective atmosphere continuously filled with argon gas at a flow rate of 10 L/min. The ultrasonic vibration frequency was set to 20 kHz. The ultrasonic power was set to 0 W (without ultrasonic vibration), 200, 400 and 600 W, respectively. Four groups of experiments were conducted according to the applied ultrasonic vibration power, and the corresponding laser cladding coating samples were marked as P0, P1, P2 and P3, respectively.

Table 1. Experimental parameters of ultrasonic vibration-assisted laser cladding.

Sample Mark	Ultrasonic Vibration Parameters		Laser Cladding Process Parameters		
	Ultrasonic Power (W)	Frequency (kHz)	Laser Power (W)	Scanning Speed (mm/s)	Spot Diameter (mm)
P0	0				
P1	200				
P2	400	20	450	3	1
P3	600				

2.4. Coating Properties Test Methods

The phase compositions of the coating surface were analyzed using an X-ray diffractometer (XRD, Advance D8, Bruker, Berne, Switzerland) with Cu Kα (40 kV, 40 mA) radiation, and X-ray spectra were acquired in the 2θ range of 20° to 80° using a scanning speed of 2°/min.

Before observation, the coated samples were wire-cut into cross-sectional test pieces of size 15 mm × 6 mm × 6 mm, and polished by SiC polishing paper, and then etched with corrosive solution (HNO$_3$: HF: H$_2$O = 1:3:9, vol) for 20 s. The purity of nitric acid solution is analytical purity, and the concentration is 65%. The purity of hydrofluoric acid solution is analytical purity, and the concentration is 40%. A scanning electronic microscopy (SEM, MIRA3 TESCAN, TESCAN Co., Brno, CZE), attached with an energy dispersive spectroscopy (EDS, Oxford Inc., Oxford, UK) system, was used to observe the microstructure characteristics and element distribution of the coatings fabricated with or without ultrasonic vibration.

The micro-hardness of the coating cross-section was measured using a Vickers hardness tester (HVS-1000Z, Vegour, Shanghai, China). The test load was 200 g and the holding time was 10 s. Starting from the coating top surface, a point was measured at 50 μm intervals along the depth direction. In order to reduce the measurement error, the measurement was repeated three times at the same horizontal position with an interval of 100 μm, and the average value was calculated as the micro-hardness at this depth.

The friction and wear properties of the coatings were tested in simulated body fluid (SBF) using a ball-on-disc friction and wear tester (TRB3, Anton Paar, Berne, Switzerland). As shown in Figure 3, the Si$_3$N$_4$ ceramic grinding balls (6 mm diameter) as counter-face material were used for the friction and wear test; the applied normal load was 10 N; the motion of the grinding balls had a rotational radius of 3 mm and a speed of 200 rpm; the ambient temperature was set at 36.5 ± 1 °C; and the duration of the wear test was 90 min. To avoid experimental error, three replicated test pieces were tested for each sample under the same test conditions. The wear cross-sectional profile of the worn track on the test piece

was measured using a super-high magnification lens zoom 3D microscope (VHX-5000, Keyence, Osaka, Japan). Eight points were measured for each worn track and the average value was taken as the wear cross-section profile. The wear volume loss was calculated by Equation (1):

$$V = 2\pi r \times A \tag{1}$$

where V is the wear volume loss; r is the radius of the worn track; and A is the average value of the wear cross-sectional area.
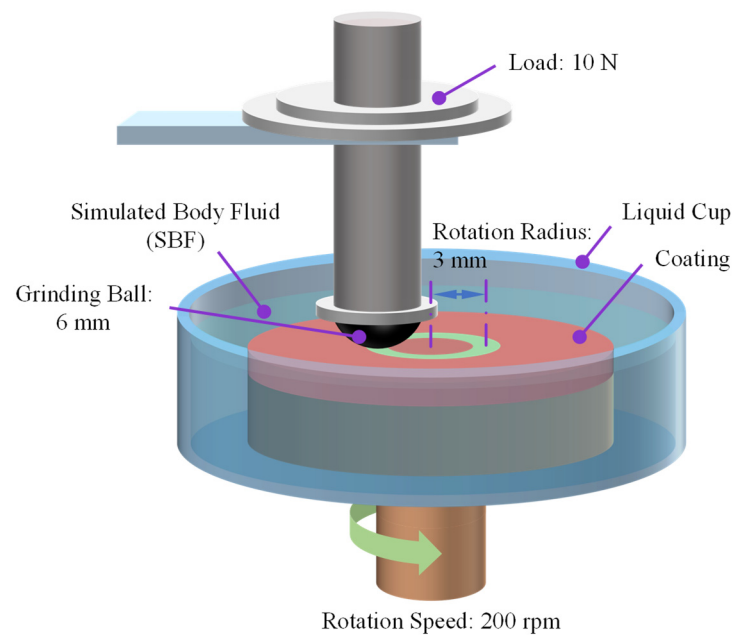
Figure 3. Schematic diagram of friction and wear test.

The elastic modulus of the coatings was tested using an in-situ nanomechanical test system (Agilent G200, Agilent Inc., Santa Clara, CA, USA) under the continuous stiffness mode (CSM) combined with a trigonal diamond Berkovich indenter (Guangzhou Zhicheng Technology Co., Ltd., Guangzhou, China). The maximum indentation depth of the test was set to 1000 nm, and unloaded after reaching the set depth. Four indentation points were measured for each sample and the average value was taken as the elastic modulus.

The residual stress in the coating surface was measured by the $\sin^2\psi$ method using an X-ray stress diffractometer (advance D8, Cu radiation, 40 kV, 40 mA, Bruker, Berne, Switzerland). The TiC (311) crystal plane was used as the diffraction plane, and the diffraction angle was about 73°. The samples were totally measured for 12 points, whose rotation angle ranges from −45° to 0° and 0° to 45° with an interval of 9°. Under the same test parameters, three parallel test pieces were tested for each sample.

3. Results and Discussion

3.1. Effect of Ultrasonic Vibration on Morphology of Coating's Cross-Section

Figure 4 shows the cross-section morphology images of the coatings fabricated at different ultrasonic vibration power. Figure 4a,e show that the surface of the P0-Coating fabricated without ultrasonic vibration showed a wavy concave contour with obvious overlapping characteristics, and there were some pores at the interface between the coating and the substrate. Figure 4b,f show that when the ultrasonic power was 200 W, the height difference between the center and edge of the concave contour of P1-Coating surface decreased, and the number of pores in the coating began to decrease. Figure 4c,g show that when the ultrasonic power was 400 W, the surface height difference of P2-Coating basically disappeared, the surface appeared flat, and the number of pores in the coating was significantly reduced. Figure 4d,h show that when the ultrasonic power was 600 W,

the height difference of the P3-Coating surface began to appear again. In summary, the top surface of the coating fabricated with ultrasonic vibration applied was more uniform, the height differences between the cladding tracks were reduced, the coating's surface morphology was greatly improved, and the number of pores in the coating was also greatly reduced. Among them, when the ultrasonic power was 400 W (P2-Coating), the surface of the coating became flat and the number of pores was significantly reduced. Due to the superposition of the acoustic streaming effect and cavitation effect of ultrasonic vibration, when the ultrasonic wave propagated into the molten pool and acted on the viscous molten medium, it would lead to a reduction of ultrasonic amplitude and generate acoustic pressure gradient [24]. This generates volume driving force in the ultrasonic propagation direction, which promotes the rapid flow of molten medium in the molten pool and makes the gas in the molten pool escape in time; simultaneously, the cavitation effect of ultrasonic vibration increases the wettability of the molten medium [21], resulting in an improvement of the coating morphological quality.
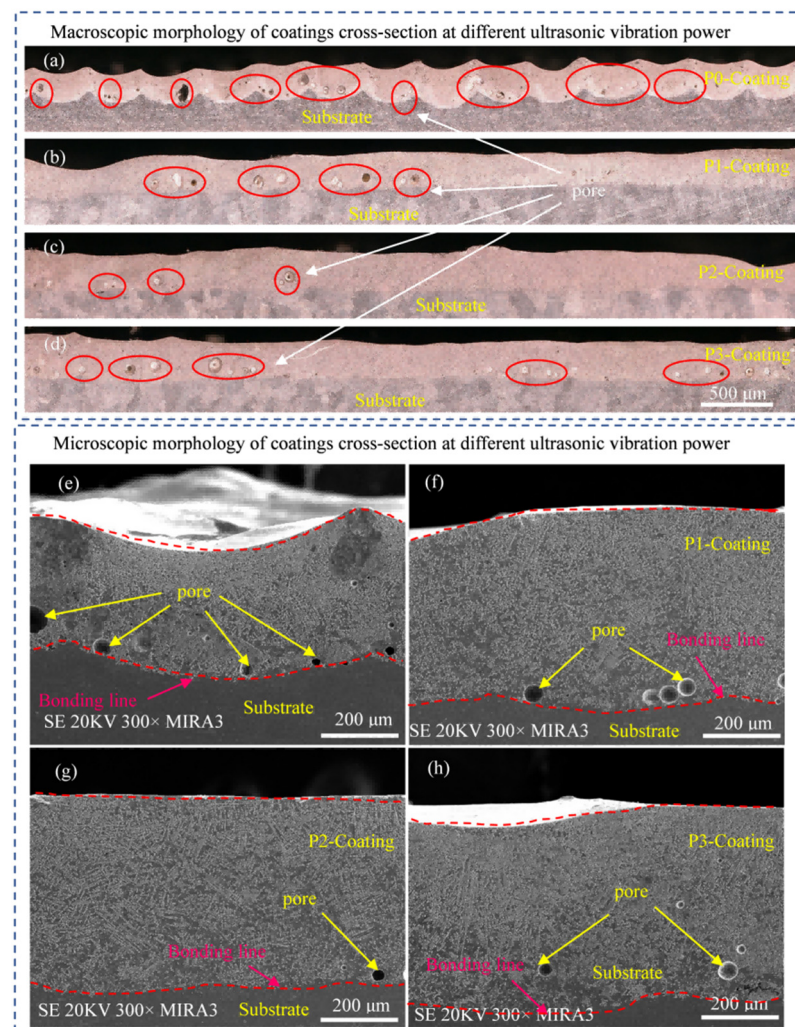

Figure 4. The cross-section morphology images of coatings fabricated with different ultrasonic vibration power: Macroscopic: (**a**) P0-Coating, (**b**) P1-Coating, (**c**) P2-Coating, (**d**) P3-Coating; Microscopic: (**e**) P0-Coating, (**f**) P1-Coating, (**g**) P2-Coating, (**h**) P3-Coating.

3.2. Effect of Ultrasonic Vibration on Phase Compositions of the Coatings

In order to analyze the effect of ultrasonic vibration on the phase compositions of the coating, the coatings were analyzed by XRD, and the XRD pattern were shown in Figure 5. The diffraction peaks (2 theta) of the coatings were consistent with the 2 theta of

TiC (No. 65-8805), TiB (No. 73-2148), α-Ti (No. 89-5009), AlTi$_3$ (No. 52-0859) and TiVC$_2$ (No. 65-7931) in the standard data card of the Joint Committee on Powder Diffraction Standards (JCPDS). The analysis results showed that the coatings fabricated with different ultrasonic vibration powers were all mainly composed of TiC, TiB, α-Ti, AlTi$_3$ and TiVC$_2$. However, the intensity ratios of the diffraction peaks on the (220) and (311) crystal planes of TiC decreased in the coating fabricated with ultrasonic vibration, which may be the change in the direction of heat flow inside the molten pool caused by ultrasonic vibration, resulting in a change in the orientation of the crystal plane [25].
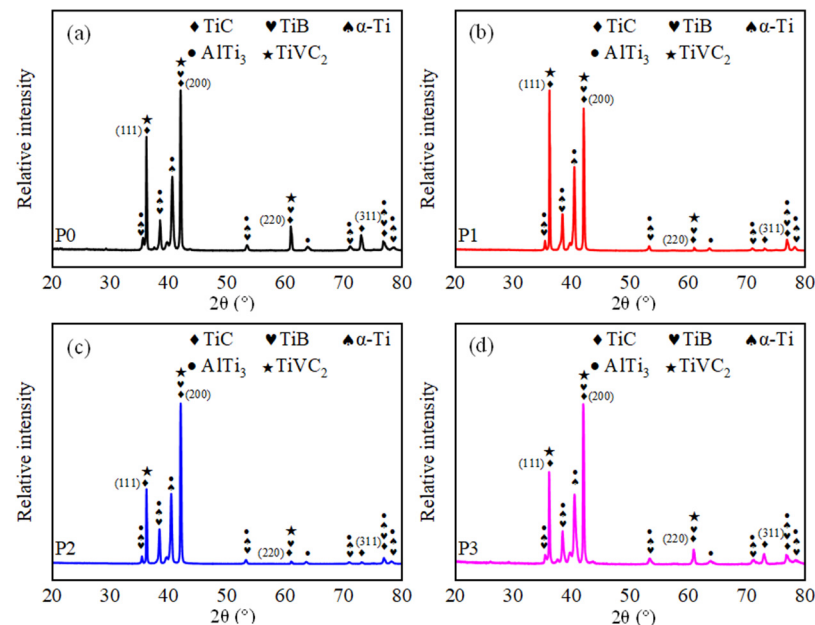
Figure 5. XRD pattern of ceramic coatings fabricated with different ultrasonic power: (**a**) P0-Coating, (**b**) P1-Coating, (**c**) P2-Coating, (**d**) P3-Coating.

According to the JCPDS cards (TiC, No. 65-8805), (TiB, No. 73-2148) and (α-Ti, No. 89-5009), it was known that the three main diffraction peaks of TiC correspond to 2θ ≈ 36.2°, 42.0° and 60.9°, and the corresponding crystal planes were (111), (200) and (220), respectively; the three main diffraction peaks of TiB correspond to 2θ ≈ 35.6°, 38.5° and 71.0°, and the corresponding crystal planes were (011), (111) and (113), respectively; and the three main diffraction peaks of α-Ti correspond to 2θ ≈ 40.6°, 53.4° and 78.3°, and the corresponding crystal planes were (101), (102) and (112), respectively. The relative contents of Ti, TiC and TiB phases in the coating fabricated with different ultrasonic vibration powers were obtained by semi-quantitative analysis with Jade 6.0 software, as shown in Figure 6. It was shown that the relative contents of Ti in P0-Coating, P1-Coating, P2-Coating, and P3-Coating were 17.4 wt.%, 13.7 wt.%, 14.0 wt.%, and 19.3 wt.%, respectively; the relative contents of TiC were 38.2 wt.%, 60.7 wt.%, 59.0 wt.%, and 32.7 wt.%, respectively; and the relative contents of TiB were 44.4 wt.%, 25.6 wt.%, 27.0 wt.%, and 48.0 wt.%, respectively. The relative content of the ceramic phases (TiC, TiB) in the coating was 82.6 wt.% when no ultrasonic vibration was applied. The relative content of the ceramic phases in the coating was about 86.0 wt.% when the ultrasonic power was 200 and 400 W. While the relative content of the ceramic phases decreased back to about 80.0 wt.% when the ultrasonic power was 600 W. In conclusion, choosing the appropriate ultrasonic power could increase the ceramic phase content in the coating and reduce the dilution rate, which was theoretically beneficial to improve the mechanical properties of the ceramic coatings.
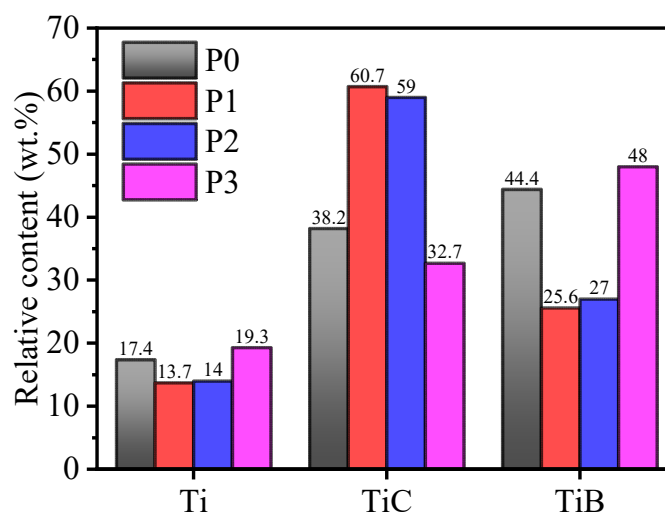
Figure 6. Relative contents of Ti, TiC and TiB phases in coatings fabricated with different ultrasonic power.

### 3.3. Effect of Ultrasonic Vibration on Microstructure of the Coatings

The SEM images on cross-section of TiC/TiB composite ceramic coatings fabricated without or with ultrasonic vibration are shown in Figure 7. It is observed from Figure 7a that there were mostly dendrites and a few granular crystal grains in the P0-Coating fabricated without ultrasonic vibration, and most of the granular crystals were attached around the dendrites. As shown in Figure 7b–d, when the ultrasonic power was 200 W, the dendrites in P1-Coating started to be broken; when the ultrasonic power was 400 W, the dendrites in P2-Coating were broken and turned into fine granular crystal grains; when the ultrasonic power was 600 W, the dendrites in P3-Coating were broken and also turned into granular crystal grains, but the granular crystal grains obviously became significantly coarser. The results showed that the dendrites in the coating were gradually broken, and the granular crystals became coarser with the increase of ultrasonic vibration power. The reason for the coarsening of the grains can be attributed to the fact that under the action of high-intensity ultrasonic vibration, the cycle of laser cladding powder to form a molten pool and cooling solidification was prolonged, meanwhile, the grains in the molten state were continuously broken and remelted during the period, which led to the coarser crystal grains obtained. It can be concluded that the effect of ultrasonic vibration applied in the laser cladding process on the TiC/TiB composite ceramic coating was to break the dendrites and turn them into granular crystal grains.

To further investigate the effect of the applied ultrasonic vibration on the TiC/TiB composite ceramic coating formation mechanism, the typical grain morphology in P0-coating and P3-coating were analyzed by EDS spot scanning energy spectrum analysis. Among them, Spectrum 1 at a typical granular crystal grain in P0-Coating, Spectrum 2 at a typical dendrite in P0-Coating, Spectrum 3 at a typical granular crystal grain in P3-Coating, and Spectrum 4 at a typical granular crystal grain from a broken dendrite in P3-Coating. The corresponding EDS spot scanning energy spectrum analysis results were shown in Figure 8 and Table 2. The Ti/C ratio of the granular crystal grain (Spectrum 1 at P0-Coating) was 1.2, and the granular crystal grain did not contain B element; the Ti/C ratio of the dendrite (Spectrum 2 at P0-Coating) was 1.9, and the Ti/B ratio was 0.8. The Ti/C ratio of the granular crystal grain (Spectrum 3 at P3-Coating) was 1.3, and the granular crystal grain did not contain B element either; the Ti/C ratio of the typical granular crystal grain from a broken dendrite (Spectrum 4 at P3-Coating) was 1.3, and the Ti/B ratio was 0.9. As can be seen from the above results, the Ti/C ratios of Spectrum 1 and Spectrum 3 were similar, and neither of them contained B element; while the Ti/B ratios of Spectrum 2 and Spectrum 4 were similar. According to the XRD results in the previous Section 3.2 (Figure 5) and the EDS analysis results, since the crystal grains contain almost no V element, and Ti,

B, and C elements in the coating formed TiB and TiC ceramic phases, therefore, it could be determined that the dendritic crystal in in P0-Coating was composed of TiB, while granular crystal in P0-Coating was composed of TiC, respectively; the phase of granular crystal in P3-Coating was partly broken TiB grains, and the other part was TiC which existed as granular crystal itself. That is, the transformation of TiB phase from dendrite to granular crystal grain was only a change in grain size, and the phase composition of the grains did not change.
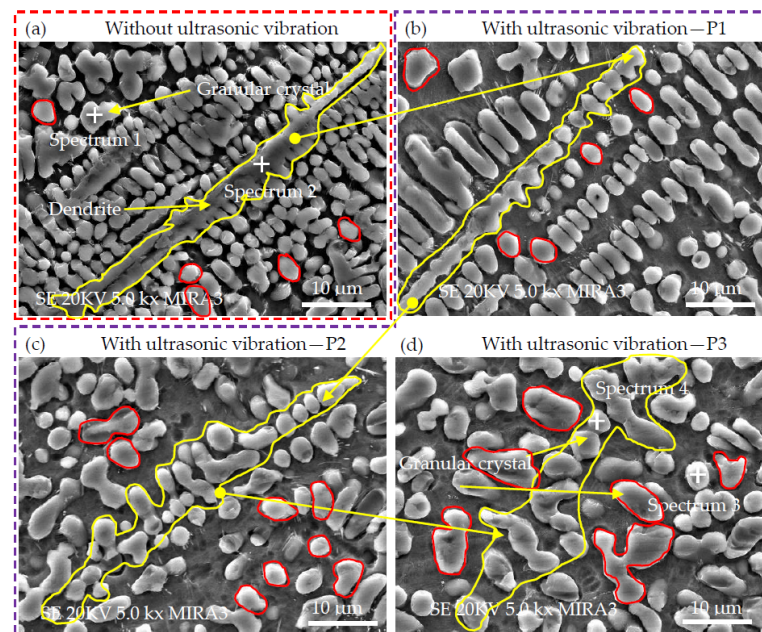
Figure 7. Effect of ultrasonic vibration power on the microstructure of TiC/TiB composite ceramic coating: (**a**) P0-Coating, (**b**) P1-Coating, (**c**) P2-Coating, (**d**) P3-Coating.
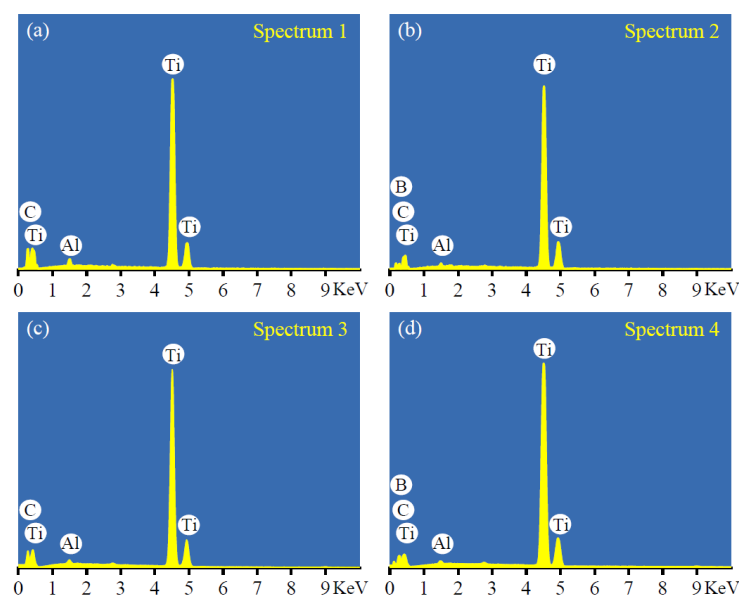

Figure 8. EDS spot scanning energy spectrum analysis results: (**a**) Spectrum 1 in Figure 7a, (**b**) Spectrum 2 in Figure 7a, (**c**) Spectrum 3 in Figure 7d, (**d**) Spectrum 4 in Figure 7d.

Figure 9 shows the main effect mechanism of ultrasonic vibration changing the microstructure of laser cladding coating, including the initial cavitation bubble, cavitation bubble oscillation, cavitation bubble collapse, and dendrite fracture. The ultrasonic cavita-

tion effect caused the cavitation bubble in the molten pool to collapse [26], the high-speed micro-shock wave was generated at the moment of bubble collapse [27], high-speed microjets caused by micro-shock wave broke the growing TiB dendrites, and then many TiB granular crystal grains formed.

Table 2. EDS spot scanning energy spectrum analysis results (Atomic%).

| Sample	Spectrum	Ti	C	B	Al	V	Ti/C	Ti/B
P0-Coating	Spectrum 1	52.7	45.6	-	1.7	-	1.2	-
	Spectrum 2	36.2	18.6	44.8	-	0.4	1.9	0.8
P3-Coating	Spectrum 3	55.6	43.4	-	1.1	-	1.3	-
	Spectrum 4	34.2	26.9	38.2	-	0.5	1.3	0.9
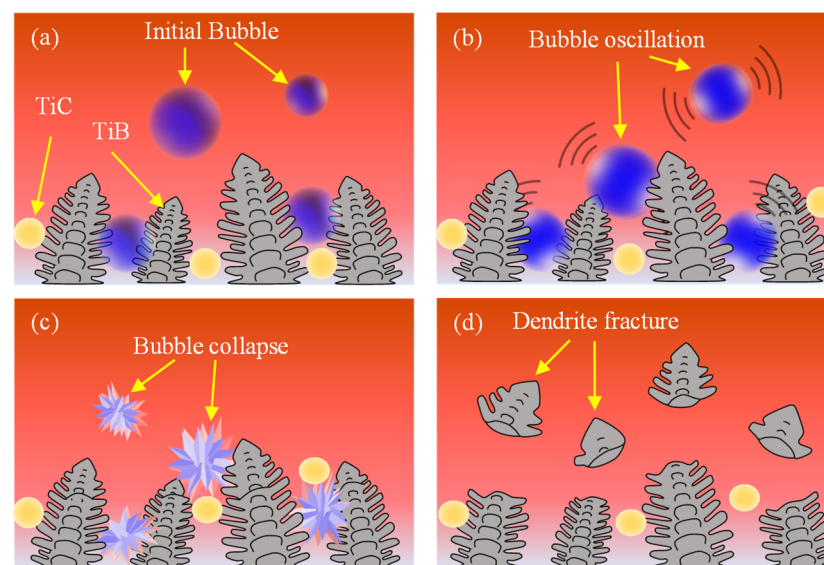
Figure 9. The main effect mechanism of ultrasonic vibration changing the microstructure of laser cladding coating: (**a**) Initial cavitation bubble, (**b**) Cavitation bubble oscillation, (**c**) Cavitation bubble collapse, (**d**) Dendrite fracture.

3.4. Effect of Ultrasonic Vibration on Micro-Hardness and Wear Resistance of the Coatings

The micro-hardness distribution curves of the coatings fabricated with different ultrasonic vibration power along the depth direction are shown in Figure 10a, and the average micro-hardness values of the coated zones are shown in Figure 10b. It can be seen that the micro-hardness of the coatings fabricated with ultrasonic vibration was higher than that of the coating fabricated without ultrasonic vibration. The average micro-hardness of P0-Coating fabricated without ultrasonic vibration was 758 $HV_{0.2}$, and the average micro-hardness of P1-Coating, P2-Coating and P3-Coating fabricated with ultrasonic vibration were 836.4, 896.1 and 785.9 $HV_{0.2}$, respectively. When the ultrasonic power was increased from 200 to 400 W, the micro-hardness of the coating increased. However, when the ultrasonic power was further increased to 600 W, the micro-hardness of the coating decreased. In general, the ultrasonic vibration had the effect of improving the micro-hardness of the coating.

Figure 11 shows the effect of ultrasonic vibration power on friction coefficient of laser cladding ceramic coating. The average friction coefficient of P0-Coating fabricated without ultrasonic vibration was 0.32, and the average friction coefficients of P1-Coating, P2-Coating, and P3-Coating fabricated with ultrasonic vibration were 0.28, 0.16, and 0.48, respectively. It can be seen that the friction coefficient of the coating fabricated with ultrasonic vibration at power of 400 W was only 50% that of the coating fabricated without ultrasonic vibration, while the friction coefficient of the coating fabricated with ultrasonic

vibration at power of 600 W increased by 50% compared with that of the coating fabricated without ultrasonic vibration. In other words, an appropriate ultrasonic vibration power had an obvious positive effect on reducing the friction coefficient of the coating. According to Figures 6 and 7c, the decrease in friction coefficient of the coatings fabricated with ultrasonic vibration at appropriate power could be attributed to the refinement of ceramic crystal grains and the increase in ceramic phase content that increased the micro-hardness of the coating, which reduced the contact area between the grinding ball and the coating, thus reducing the friction coefficient of the coatings. When the ultrasonic vibration power increased from 400 to 600 W, the friction coefficient of the coating increased and exceeded that of the coating fabricated without ultrasonic vibration. The main reason should be the coarsening of crystal grains in the coating under the action of the higher intensity ultrasonic vibration. It can be concluded that P2-Coating fabricated with ultrasonic vibration at power of 400 W had the lowest friction coefficient.
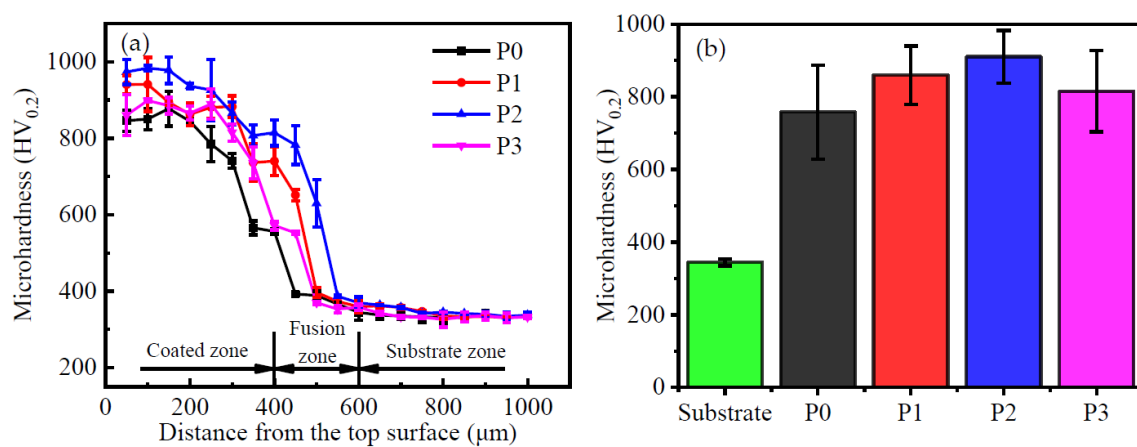
Figure 10. (**a**) Micro-hardness distribution curves of coatings fabricated with different ultrasonic vibration power along the depth direction, (**b**) The average micro-hardness values of the coated zones.
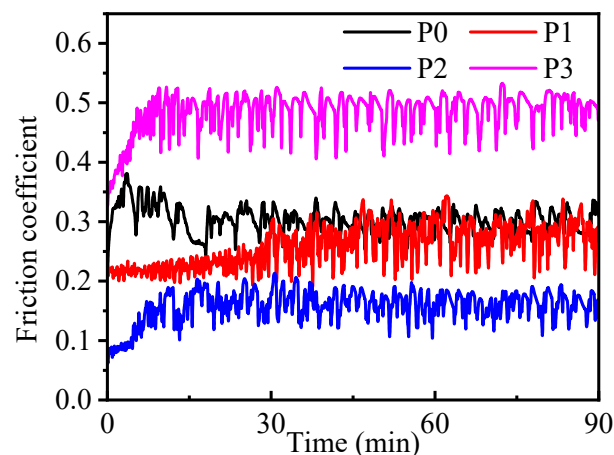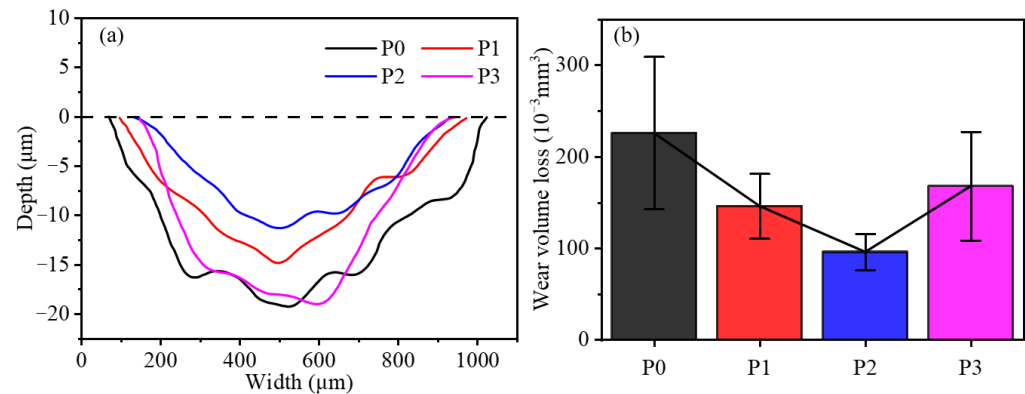

Figure 11. The effect of ultrasonic vibration power on friction coefficient of laser cladding ceramic coatings.

The effect of ultrasonic vibration power on wear resistance of laser cladding ceramic coating is shown in Figure 12a. The profile width and depth of the wear tracks on the coatings fabricated with ultrasonic vibration were less than that of the coating fabricated without ultrasonic vibration. The wear volumes loss of coatings fabricated with different ultrasonic vibration power are shown in Figure 12b. The wear volume loss of the coating fabricated without ultrasonic vibration was 2.31×10^{-1} mm^3, while the wear volumes of the coatings fabricated with ultrasonic vibration were reduced to 1.44×10^{-1}, 1.02×10^{-1} and 1.61×10^{-1} mm^3, respectively. Compared with the coating fabricated

without ultrasonic vibration, the wear volume of the coatings fabricated with ultrasonic vibration decreased by 37.8%, 127.35% and 30.4%, respectively. It can be seen that P2-Coating fabricated with ultrasonic vibration at power of 400 W had the best wear resistance.

Figure 12. The effect of ultrasonic vibration power on wear of laser cladding ceramic coatings: (**a**) wear track profile, (**b**) wear volume loss.

According to the theory of Holm–Archard wear law [28], under the condition of constant load and sliding distance, the wear volume loss is inversely proportional to the material surface hardness and directly proportional to the coefficient of friction, that is, the greater the material surface hardness and the smaller the friction coefficient, the less the wear volume loss, as shown in Equation (2).

$$V_W = \frac{KFL}{HV} \tag{2}$$

where V_W is the wear volume loss, K is the friction coefficient, F is the load, L is the sliding distance, and HV is the hardness of the material.

When the ultrasonic vibration power increased from 200 to 400 W, the surface micro-hardness of the coating increased, the friction coefficient decreased, and hence the wear volume loss of the coating decreased. However, when the ultrasonic vibration power was increased to 600 W, the micro-hardness of the coating decreased and the friction coefficient increased, resulting in an increase to the wear volume loss of the coating. In general, the wear resistance of the coating was improved due to the application of ultrasonic vibration. The main reason was that the ultrasonic vibration could synthesize more ceramic phase in situ, refine the crystal grains of the coating, and promote a more uniform distribution of the ceramic phase in the coating.

The wear morphology images of the coatings prepared by laser cladding assisted with different ultrasonic vibration power are shown in Figure 13. It is observed that the worn surfaces were all characterized by shallow grooves with parallel and discontinuous furrows, and a few spalling pits. The wear mechanism of the coating surface is shown in Figure 14. Since the hardness of Si_3N_4 ceramic grinding ball was higher than that of the coating surface, the coating surface was cut by micro-convex bodies on the ball surface, forming furrows on the coating surface and producing wear debris. The wear debris were trapped between the sliding surfaces, the wear mechanism gradually changed from abrasive two-body wear to abrasive three-body wear in the process of the reciprocal cycle friction. During the three-body wear process, the wear debris were covered on the coating surface by repeated crushing under the action of friction load, which caused plastic deformation of the micro-convex bodies on the coating surface, and fatigue cracks began to initiate on the coating surface. With the action of alternating stress for a long time, the fatigue cracks initiated on the coating surface further expand, which resulted in the peeling of the fatigue layer and fatigue wear on the coating surface. In summary, the application of

ultrasonic vibration for laser cladding coating did not affect the wear mechanisms of the coatings, which were abrasive wear and fatigue wear.
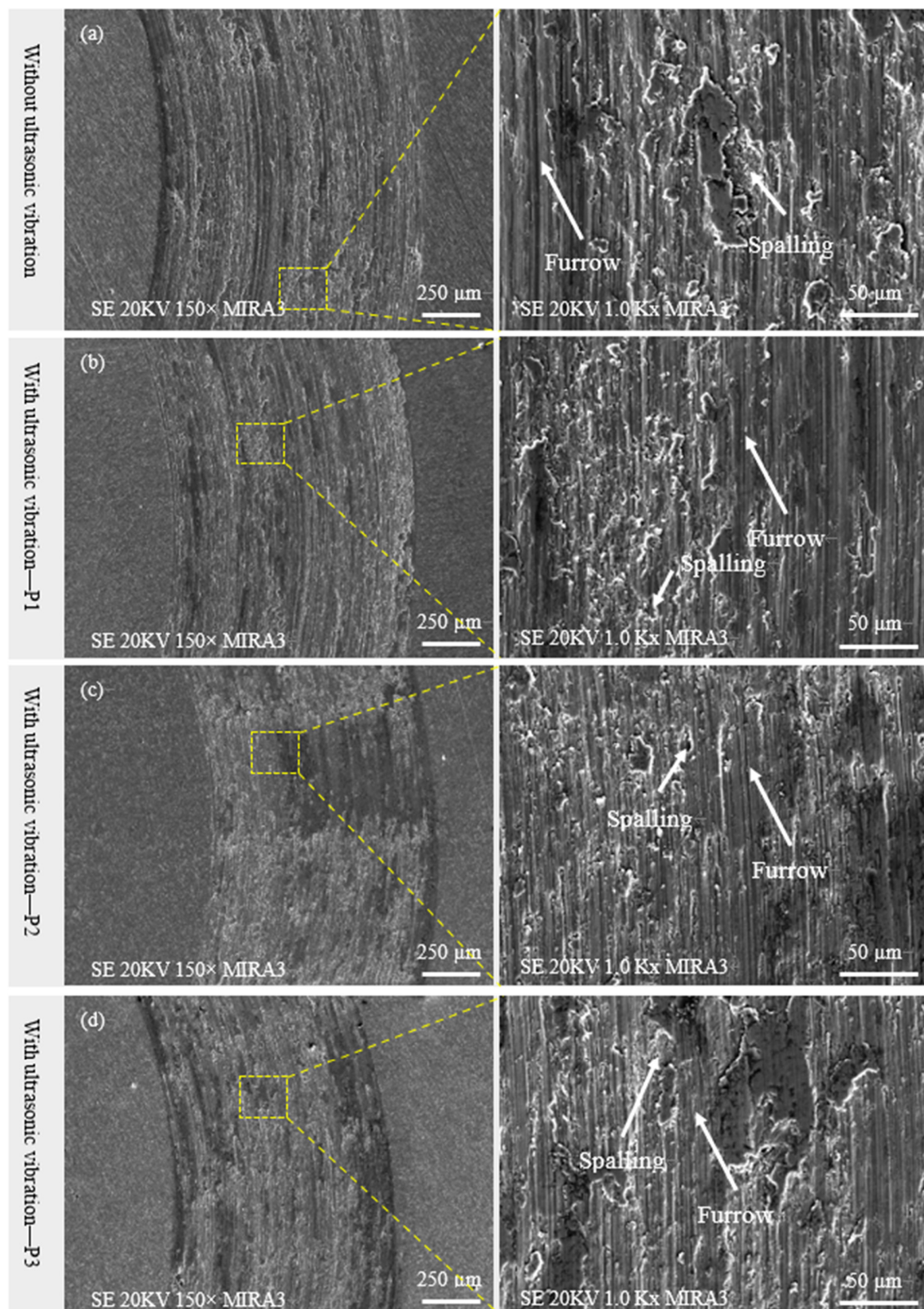

Figure 13. Wear morphology images of coatings prepared by laser cladding assisted with different ultrasonic vibration power: (**a**) P0-Coating, (**b**) P1-Coating, (**c**) P2-Coating, (**d**) P3-Coating.
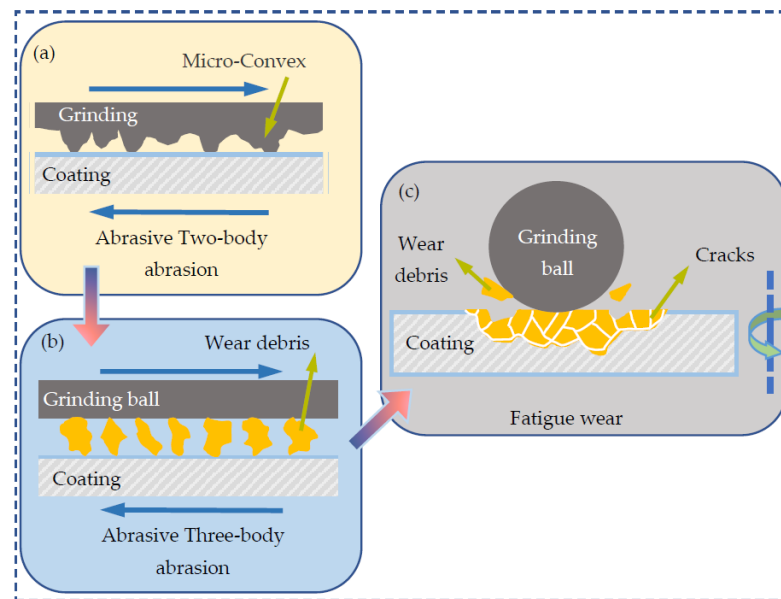
Figure 14. Schematic diagram of wear mechanism transformation of laser cladding ceramic coating: (**a**) Abrasive two-body wear, (**b**) Abrasive three-body wear, (**c**) Fatigue wear.

3.5. Effect of Ultrasonic Vibration on Residual Stress of the Coatings

The modulus of elasticity is an important parameter for measuring residual stresses in coatings by X-ray diffraction [29]. Therefore, the elastic modulus of the coating was measured using the same sample by nano indentation after nondestructive measurement of residual stress on the coating surface using X-ray. Figure 15 shows the load-displacement relationship curves by nano indentation for the coatings fabricated with different ultrasonic vibration power by nano indentation. In order to avoid the effect of surface hardening on the nano indentation results, the 800–1000 nm displacements in the loading stage were chosen to calculate the elastic modulus of the coating. The elastic modulus values of the coatings were calculated by Oliver–Pharr method [30], as shown in Table 3.
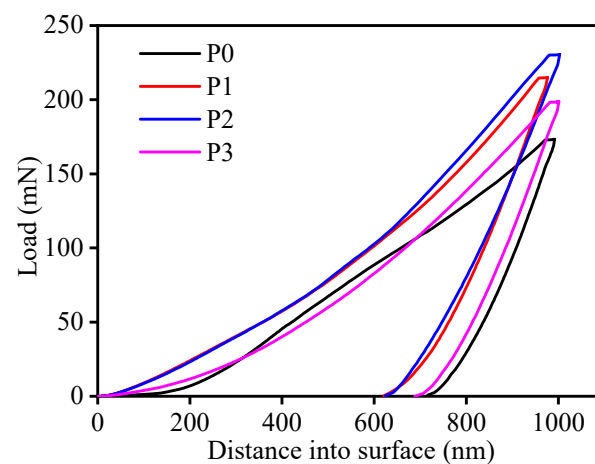

Figure 15. Load-displacement curves of coatings fabricated with different ultrasonic vibration power.

Table 3. Elastic modulus of coatings fabricated with different ultrasonic vibration power.

Sample	P0	P1	P2	P3
Elastic modulus (GPa)	225	243	231	230

If there is residual stress on the coating, the position of diffraction peak will change when Bragg diffraction occurs. The shift distance of diffraction peak position is related to the stress [31]. Generally, only one diffraction peak can be selected to measure the residual stress of composite coating, and it is better to choose a diffraction peak of single phase. Since the diffraction peak intensity of TiB phase in the coating was not high and overlapped with the diffraction peaks of other phases, the diffraction peak of TiC phase was selected to measure the residual stress of the coatings. Therefore, an X-ray stress diffractometer (advance D8, Cu radiation, 40 kV, 40 mA) was used to measure the displacement of TiC diffraction peak, and then the residual stress on the coating surface was obtained by calculating.

The relationship between residual stress on the coating surface and ultrasonic vibration power is shown in Figure 16. It is observed that there existed residual tensile stress on all coating surfaces. The residual tensile stress was 1.60 GPa in P0-Coating fabricated without ultrasonic vibration, and 1.89, 1.59, and 1.12 GPa in P1-Coating, P2-Coating, and P3-Coating fabricated with different ultrasonic vibration power, respectively.
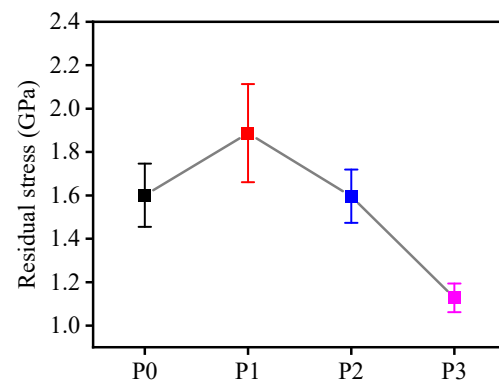
Figure 16. Relationship between residual stress on the coating surface and ultrasonic vibration power.

Among them, the residual tensile stress of the coating fabricated with ultrasonic vibration at power of 200 W was larger than that of the coating fabricated without ultrasonic vibration. When the ultrasonic vibration power was 200 W, the cavitation effect on the molten pool was relatively weak, resulting in that only part of the initial developed dendrites in the molten pool were broken, and the dendrites were interlaced with each other, thus forming a more chaotic and closed dendrite network, as shown in Figure 7b. Meanwhile, due to the poor stirring caused by the acoustic streaming effect under low ultrasonic power in the molten pool, the molten mass among the disorderly closed dendrite networks could not be replenished in time during the solidification of the molten pool, resulting in different solidification shrinkage rates and larger residual tensile stress. Under the combination of these two factors, the residual tensile stress on the coating fabricated with low ultrasonic vibration power was larger than that of the coating fabricated without ultrasonic vibration.

However, as the ultrasonic vibration power further increased, the residual tensile stress in the coating decreased. The cavitation effect increased with the increase in ultrasonic vibration power, so that the developed dendrites were completely broken and the tensile stresses between dendrites was reduced. At the same time, the acoustic streaming effect of ultrasonic made the temperature and structure distribution of molten pool more uniform, which effectively reduced the tensile stress of the coating during solidification. The reduction in residual tensile stress plays a significant role in inhibiting the initiation and propagation of cracks, which can improve the fatigue resistance of the coating on the bearing part of the artificial articular surface [32]. As a result, the coatings prepared by ultrasonic vibration assistance were more able to prevent crack initiation and improve the fatigue strength of the coatings.

4. Conclusions

TiC/TiB composite ceramic coatings were in-situ synthesized by ultrasonic vibration-assisted laser cladding process, and the effects of ultrasonic vibration on the microstructure and mechanical properties of ceramic coatings were described. The application of ultrasonic vibration power of 400 W could improve the quality of the coatings and mechanical properties. The main conclusions of the study are as following:

1. The dendrites in the coating were broken by ultrasonic cavitation effect, and gradually turned into granular crystal grains with the increase of ultrasonic vibration power.
2. The ultrasonic vibration introduced into the laser cladding process could increase the relative content of the ceramic phase (TiC, TiB) in the coating. The relative content of ceramic phases in the coating fabricated with ultrasonic vibration at power of 400 W was the highest at about 86.0 wt.%.
3. The ultrasonic vibration introduced into the laser cladding process improved the tribological properties of the coating. The wear resistance of the coating fabricated with ultrasonic vibration power 400 W was about 1.2 times higher, and the friction coefficient was 50% lower than that of the coating fabricated without ultrasonic vibration.

References

1. Kaur, M.; Singh, K. Review on titanium and titanium based alloys as biomaterials for orthopaedic applications. *Mater. Sci. Eng. C* **2019**, *102*, 844–862. [CrossRef] [PubMed]
2. Ibrahim, M.Z.; Sarhan, A.A.; Yusuf, F.; Hamdi, M. Biomedical materials and techniques to improve the tribological, mechanical and biomedical properties of orthopedic implants—A review article. *J. Alloys Compd.* **2017**, *714*, 636–667. [CrossRef]
3. Mahajan, A.; Devgan, S.; Sidhu, S.S. Surface alteration of biomedical alloys by electrical discharge treatment for enhancing the electrochemical corrosion, tribological and biological performances. *Surf. Coat. Technol.* **2021**, *405*, 126583. [CrossRef]
4. Perumal, G.; Geetha, M.; Asokamani, R.; Alagumurthi, N. Wear studies on plasma sprayed Al_2O_3–40 wt% 8YSZ composite ceramic coating on Ti–6Al–4V alloy used for biomedical applications. *Wear* **2014**, *311*, 101–113. [CrossRef]
5. Pham, D.Q.; Berndt, C.C.; Cizek, J.; Gbureck, U.; Zreiqat, H.; Lu, Z.; Ang, A.S.M. Baghdadite coating formed by hybrid water-stabilized plasma spray for bioceramic applications: Mechanical and biological evaluations. *Mater. Sci. Eng. C* **2021**, *122*, 111873. [CrossRef] [PubMed]
6. Singh, H.; Kumar, R.; Prakash, C.; Singh, S. HA-based coating by plasma spray techniques on titanium alloy for orthopedic applications. *Mater. Today Proc.* **2021**. [CrossRef]
7. Salehi, S.; Kharaziha, M.; Salehi, M. Multifunctional plasma-sprayed nanocomposite coating based on FA-ZnO-GO with improved bioactivity and wear behaviour. *Surf. Coat. Technol.* **2020**, *404*, 126472. [CrossRef]
8. Ibrahim, M.Z.; Sarhan, A.A.; Kuo, T.; Hamdi, M.; Yusof, F.; Chien, C.; Chang, C.; Lee, T. Advancement of the artificial amorphous-crystalline structure of laser cladded FeCrMoCB on nickel-free stainless-steel for bone-implants. *Mater. Chem. Phys.* **2019**, *227*, 358–367. [CrossRef]
9. Guo, Y.; Li, X.; Liu, Q. A novel biomedical high-entropy alloy and its laser-clad coating designed by a cluster-plus-glue-atom model. *Mater. Des.* **2020**, *196*, 109085. [CrossRef]

10. Ibrahim, M.Z.; Sarhan, A.A.; Kuo, T.; Yusof, F.; Hamdi, M.; Lee, T. Developing a new laser cladded FeCrMoCB metallic glass layer on nickel-free stainless-steel as a potential superior wear-resistant coating for joint replacement implants. *Surf. Coat. Technol.* **2020**, *392*, 125755. [CrossRef]

11. Jing, Z.; Cao, Q.; Jun, H. Corrosion, wear and biocompatibility of hydroxyapatite bio-functionally graded coating on titanium alloy surface prepared by laser cladding. *Ceram. Int.* **2021**, *47*, 24641–24651. [CrossRef]

12. Saeedi, R.; Razavi, R.S.; Bakhshi, S.R.; Erfanmanesh, M.; Bani, A.A. Optimization and characterization of laser cladding of NiCr and NiCr–TiC composite coatings on AISI 420 stainless steel. *Ceram. Int.* **2021**, *47*, 4097–4110. [CrossRef]

13. Fan, P.; Zhang, G. Study on process optimization of WC-Co50 cermet composite coating by laser cladding. *Int. J. Refract. Met. Hard Mater.* **2020**, *87*, 105133. [CrossRef]

14. Liu, H.; Liu, J.; Li, X.; Chen, P.; Yang, H.; Hao, J. Effect of heat treatment on phase stability and wear behavior of laser clad AlCoCrFeNiTi$_{0.8}$ high-entropy alloy coatings. *Surf. Coat. Technol.* **2020**, *392*, 125758. [CrossRef]

15. Chen, T.; Li, W.; Liu, D.; Xiong, Y.; Zhu, X. Effects of heat treatment on microstructure and mechanical properties of TiC/TiB composite bioinert ceramic coatings in-situ synthesized by laser cladding on Ti6Al4V. *Ceram. Int.* **2021**, *47*, 755–768. [CrossRef]

16. Choi, J.; Choudhuri, S.K.; Mazumder, J. Role of preheating and specific energy input on the evolution of microstructure and wear properties of laser clad Fe-Cr-C-W alloys. *J. Mater. Sci.* **2000**, *35*, 3213–3219. [CrossRef]

17. Hu, Y.; Ning, F.; Cong, W.; Li, Y.; Wang, X.; Wang, H. Ultrasonic vibration-assisted laser engineering net shaping of ZrO$_2$-Al$_2$O$_3$ bulk parts: Effects on crack suppression, microstructure, and mechanical properties. *Ceram. Int.* **2018**, *44*, 2752–2760. [CrossRef]

18. Ning, F.; Hu, Y.; Liu, Z.; Cong, W.; Li, Y.; Wang, X. Ultrasonic vibration-assisted laser engineered net shaping of Inconel 718 parts: A feasibility study. *Procedia Manuf.* **2017**, *10*, 771–778. [CrossRef]

19. Wang, H.; Hu, Y.; Ning, F.; Cong, W. Ultrasonic vibration-assisted laser engineered net shaping of Inconel 718 parts: Effects of ultrasonic frequency on microstructural and mechanical properties. *J. Mater. Process. Technol.* **2020**, *276*, 116395. [CrossRef]

20. Zhu, L.; Yang, Z.; Xin, B.; Wang, S.; Meng, G.; Ning, J.; Xue, P. Microstructure and mechanical properties of parts formed by ultrasonic vibration-assisted laser cladding of Inconel 718. *Surf. Coat. Technol.* **2021**, *410*, 126964. [CrossRef]

21. Ma, G.; Yan, S.; Wu, D.; Miao, Q.; Liu, M.; Niu, F. Microstructure evolution and mechanical properties of ultrasonic assisted laser clad yttria stabilized zirconia coating. *Ceram. Int.* **2017**, *43*, 9622–9629. [CrossRef]

22. Zhang, M.; Zhao, G.; Wang, X.; Liu, S.; Ying, W. Microstructure evolution and properties of in-situ ceramic particles reinforced Fe-based composite coating produced by ultrasonic vibration assisted laser cladding processing. *Surf. Coat. Technol.* **2020**, *403*, 126445. [CrossRef]

23. Chen, T.; Liu, D.; Wu, F.; Wang, H. Effect of CeO$_2$ on microstructure and wear resistance of TiC bioinert coatings on Ti6Al4V alloy by laser cladding. *Materials* **2018**, *11*, 58. [CrossRef] [PubMed]

24. Poncet, C.; Ferrouillat, S.; Vignal, L.; Memponteil, A.; Bulliard-Sauret, O.; Gondrexon, N. Enhancement of heat transfer in forced convection by using dual low-high frequency ultrasound. *Ultrason. Sonochem.* **2021**, *71*, 105351. [CrossRef] [PubMed]

25. Gao, J.; Li, C.; Chen, Z.; Han, X. Effect of ultrasonic vibration on the solidification behavior of laser cladding polycrystalline based on phase field method. *Mater. Rep.* **2021**, *35*, 12161–12168. [CrossRef]

26. Han, X.; Li, C.; Yang, Y.; Gao, X.; Gao, H. Experimental research on the influence of ultrasonic vibrations on the laser cladding process of a disc laser. *Surf. Coat. Technol.* **2021**, *406*, 126750. [CrossRef]

27. Ye, L.; Zhu, X.; Liu, Y. Numerical study on dual-frequency ultrasonic enhancing cavitation effect based on bubble dynamic evolution. *Ultrason. Sonochem.* **2019**, *59*, 104744. [CrossRef]

28. Almeida, R.; Börret, R.; Rimkus, W.; Harrison, D.K.; DeSilva, A.K.M. Material removal simulation for steel mould polishing. *Prod. Manuf. Res.* **2017**, *5*, 235–249. [CrossRef]

29. Morin, L.; Braham, C.; Tajdary, P.; Seddik, R.; Gonzalez, G. Reconstruction of heterogeneous surface residual-stresses in metallic materials from X-ray diffraction measurements. *Mech. Mater.* **2021**, *158*, 103882. [CrossRef]

30. Oliver, W.C.; Pharr, G.M. Measurement of hardness and elastic modulus by instrumented indentation: Advances in understanding and refinements to methodology. *J. Mater. Res.* **2004**, *19*, 3–20. [CrossRef]

31. Rossini, N.; Dassisti, M.; Benyounis, K.; Olabi, A.G. Methods of measuring residual stresses in components. *Mater. Des.* **2012**, *35*, 572–588. [CrossRef]

32. Syed, A.K.; Ahmad, B.; Guo, H.; Machry, T.; Eatock, D.; Meyer, J.; Fitzpatrick, M.E.; Zhang, X. An experimental study of residual stress and direction-dependence of fatigue crack growth behaviour in as-built and stress-relieved selective-laser-melted Ti6Al4V. *Mater. Sci. Eng. A* **2019**, *755*, 246–257. [CrossRef]